A Copper Single-Atom Cascade Bionanocatalyst for Treating Multidrug-Resistant Bacterial Diabetic Ulcer

Xin Fan, Yang Gao, Fan Yang, Jian Liang Low, Lei Wang, Beate Paulus, Yi Wang, Andrej Trampuz,* Chong Cheng,* and Rainer Haag*

Diabetic ulcers induced by multidrug-resistant (MDR) bacteria have severely endangered diabetic populations. These ulcers are very challenging to treat because the local high glucose concentration can both promote bacterial growth and limit the immune system's bactericidal action. Herein, a glucose oxidase-peroxidase (GOx-POD) dual-enzyme mimetic (DEM) bionanocatalyst, Au@CuBCats is synthesized to simultaneously control glucose concentration and bacteria in diabetic ulcers. Specifically, the AuNPs can serve as GOx mimics and catalyze the oxidation of glucose for the formation of H_2O_2; the H_2O_2 can then be further catalytically converted into OH via the POD-mimetic copper single atoms. Notably, the unique copper single atoms coordinated by one oxygen and two nitrogen atoms (CuN_2O_1) exhibit better POD catalytic performance than natural peroxidase. Further DFT calculations are conducted to study the catalytic mechanism and reveal the advantage of this CuN_2O_1 structure as compared to other copper single-atom sites. Both in vitro and in vivo experiments confirm the outstanding antibacterial therapeutic efficacy of the DEM bionanocatalyst. This new bionanocatalyst will provide essential insights for the next generation of antibiotic-free strategies for combating MDR bacterial diabetic ulcers, and also offer inspiration for designing bionanocatalytic cascading medicines.

1. Introduction

Diabetes and its complications have emerged as one of the major threats to human health, causing a large number of deaths annually.[1,2] Especially, a diabetic ulcer is one of the most serious chronic complications, featured with slow-healing wounds that are very sensitive to bacterial infections.[3] An important factor responsible for this complication is the overabundance of glucose in the wound area, which promotes the proliferation of bacteria and prevents the immune system from killing them, resulting in long-term bacterial colonization and an extremely hard-to-cure lesion.[4] To make matters worse, the emergence of multidrug-resistant (MDR) bacteria, which vitiate antibiotics' bactericidal effects, has now aggravated the situation, further endangering diabetic ulcer patients. It is therefore important to develop new strategies not only for combating MDR

X. Fan, R. Haag
Institute of Chemistry and Biochemistry
Freie Universität Berlin
Takustraße 3, 14195 Berlin, Germany
E-mail: haag@chemie.fu-berlin.de
X. Fan, L. Wang, A. Trampuz
Charité – Universitätsmedizin Berlin
Freie Universität Berlin
Humboldt-Universität zu Berlin, and Berlin Institute of Health
14195 Berlin, Germany
E-mail: andrej.trampuz@charite.de

Y. Gao
Department of Ultrasound
West China Hospital
Sichuan University
610041 Chengdu, China
F. Yang
Department of Physics
Freie Universität Berlin
Arnimallee 14, 14195 Berlin, Germany
J. L. Low, B. Paulus
Institute of Chemistry and Biochemistry
Freie Universität Berlin
Arnimallee 22, 14195 Berlin, Germany
Y. Wang
College of Materials Science and Engineering
Nanjing University of Aeronautics and Astronautics
210016 Nanjing, China
C. Cheng
College of Polymer Science and Engineering, State Key Laboratory of
Polymer Materials Engineering
Sichuan University
610065 Chengdu, China
E-mail: chong.cheng@scu.edu.cn

bacterial infections but also for controlling the glucose levels in diabetic ulcers.

Glucose oxidase (GOx) is a natural enzyme originally generated by fungi and insects.[5] Recently, it has been explored as a good candidate for treating bacterial diabetic ulcers, since it shows the ability to catalyze the glucose oxidation to generate hydrogen peroxide (H_2O_2), which is toxic to bacteria. Moreover, since glucose is one of the major nutrition sources for bacterial growth, its consumption can also lead to bacterial starvation.[6] Until now, GOx has been encapsulated in diverse matrices like hydrogel,[7–8] metal-organic frameworks,[9–11] covalent organic frameworks,[12–13] and porous silica[14] to fabricate therapeutic platforms. However, to achieve effective antibacterial efficacy, the dosage or concentration of H_2O_2 must be very high, which causes inevitable toxicity and inflammation. Recent studies have innovatively combined GOx and peroxidase (POD) in a single system in which the generated H_2O_2 can be further catalyzed into more efficient bactericidal hydroxyl radicals (•OH), thus achieving a better therapeutic effect with higher biosafety.[15–16] Nevertheless, these natural-enzyme-based therapies still face challenges due to their high synthesis cost, poor stability, and limited mass production.

Inspired by the natural POD with multiple transition metallic active sites coordinated by nitrogen and oxygen, transition-metal-based composites have been constructed and applied for diverse scenarios that require the mass generation of OH. For example, [FeIII(OH)(tpena)]+ complex was synthesized and proven to activate H_2O_2 with the formation of OH under pH 8,[17] Co_3O_4 nanoplates were synthesized as POD mimics for detecting glucose in the presence of GOx,[18] and copper-based nanozymes were designed for phenol degradation.[19] These results confirm that the transition metallic sites serve as high-performance POD mimics. However, their bioapplications are still very limited because of the potential toxicity from ion leaching. This limitation prompted us to develop bionanocatalytic medicines with single metallic atom catalytic centers; here we can not only take maximum advantage of metal, but also minimize the danger of ion leaching, since the overall dosage of metal is significantly reduced and these metallic atoms are fixed by heteroatoms in the matrix. In addition, recent studies have revealed that small gold nanoparticles (AuNPs, approved by the US Food and Drug Administration)[20] of ≈5 nm in diameter can oxidize glucose to generate gluconic acid and H_2O_2, just as GOx does.[21] Due to their high biosafety and easy synthesis, we consider AuNPs an excellent building block for constructing abiotic GOx-POD mimetic cascade catalytic platforms. To the best of our knowledge, such a rational design of dual-enzyme mimetic AuNPs/single metallic atomic bionanocatalysts for treating multidrug-resistant bacterial diabetic ulcer has not been reported until now.

In this work, we synthesized an AuNP-anchored copper single atomic bionanocatalyst (Au@CuBCats) as a novel GOx-POD dual enzyme mimetic treatment platform for bacterial diabetic ulcers. Specifically, the AuNPs can serve as GOx mimics and catalyze the oxidation of glucose for the formation of H_2O_2; the H_2O_2 can then be further catalytically converted into OH via POD-mimetic copper single atoms without extra energy input. Thus, upon the treatment with Au@CuBCats, both glucose concentration and bacterial infection in diabetic ulcers can be effectively controlled. Notably, the unique copper single atoms coordinated by one oxygen and two nitrogen atoms (CuN_2O_1) exhibit better

POD catalytic performance than natural horseradish peroxidase (HRP). Further density functional theory (DFT) calculations were conducted to facilitate a fundamental understanding of the catalytic activity and reveal the advantage of the CuN_2O_1 structure compared to other copper single-atom sites. In vitro antibacterial results demonstrate that bionanocatalysts can induce a significant bacteria-killing effect against both gram-positive and gram-negative strains. In vivo study of bacterial diabetic ulcers in a rabbit ear model confirms the outstanding therapeutic efficacy and biosafety of the bionanocatalyst. Therefore, we believe that this novel bionanocatalyst will provide essential perspectives to the next generation of antibiotic-free strategies for combating MDR bacterial infection of diabetic ulcers, and that it will also yield inspiration for designing bionanocatalytic cascading medicines.

2. Results and Discussion

The synthesis of the Au@CuBCats started with the coordination reaction of copper ions and chloranilic acid (CA), and the obtained precursors were termed as CuCA. Then, CuCA was subjected to a dicyandiamide (DCD)-assisted pyrolysis step followed by an acid etching step, producing the bionanocatalysts with abundant single-atomic copper, termed as CuBCats. Finally, the gold nanoparticles were reduced in situ on CuBCats' surface to obtain the final product, Au@CuBCats, as illustrated in **Figure 1**a. We then systematically studied the chemical and physical structures of Au@CuBCats by scanning electron microscopy (SEM), scanning transmission electron microscopy (STEM), X-ray powder diffraction (XRD), X-ray photoelectron spectroscopy (XPS) and X-ray absorption spectroscopy (XAS). Both STEM images (Figure 1b; Figure S1, Supporting Information) and SEM images (Figure S2, Supporting Information) confirmed that the bionanocatalysts had 2D structures before-and-after AuNPs loading. Meanwhile, we observed from the aberration-corrected high-angle annular dark-field scanning transmission electron microscopy images with atomic resolution (Figure 1c; Figure S3a, Supporting Information) that the isolated copper atoms were well-dispersed on the carbon matrix, where no apparent copper particle or cluster was found. Energy dispersive spectroscopy (EDS) mapping (Figure 1d; Figure S3b, Supporting Information) suggested that various elements were uniformly distributed in the bionanocatalysts. Also, the XRD pattern (Figure S4, Supporting Information) showed no copper crystal peaks; instead, the typical peaks for the (111), (200), (220), and (311) facets of AuNPs appeared, confirming the successful synthesis of Au@CuBCats.

The XPS survey scanning of CuCA-C (CuCA-C is the CuBCats without acid etching), CuBCats, and Au@CuBCats shows a clear N peak, whereas no apparent N signal was noticed for CuCA precursors, suggesting that the DCD-assisted pyrolysis facilitates N-doping (Figure S5, Supporting Information). Meanwhile, the atomic ratio of each sample has been summarized based on XPS results in Table S1 (Supporting Information). Based on the atomic ratio, the AuNPs loading rate was calculated to be 21 wt%. To understand the nitrogen atoms' bonding environment, the high-resolution XPS N1s spectra were fitted (Figure S6, Supporting Information). Here we found the highest percentage of pyridinic-N (36.17%), which plays an important role in anchoring atomic metals according to previous studies,[22–24] suggesting the formation of Cu–N_x sites. To further study the oxidation state
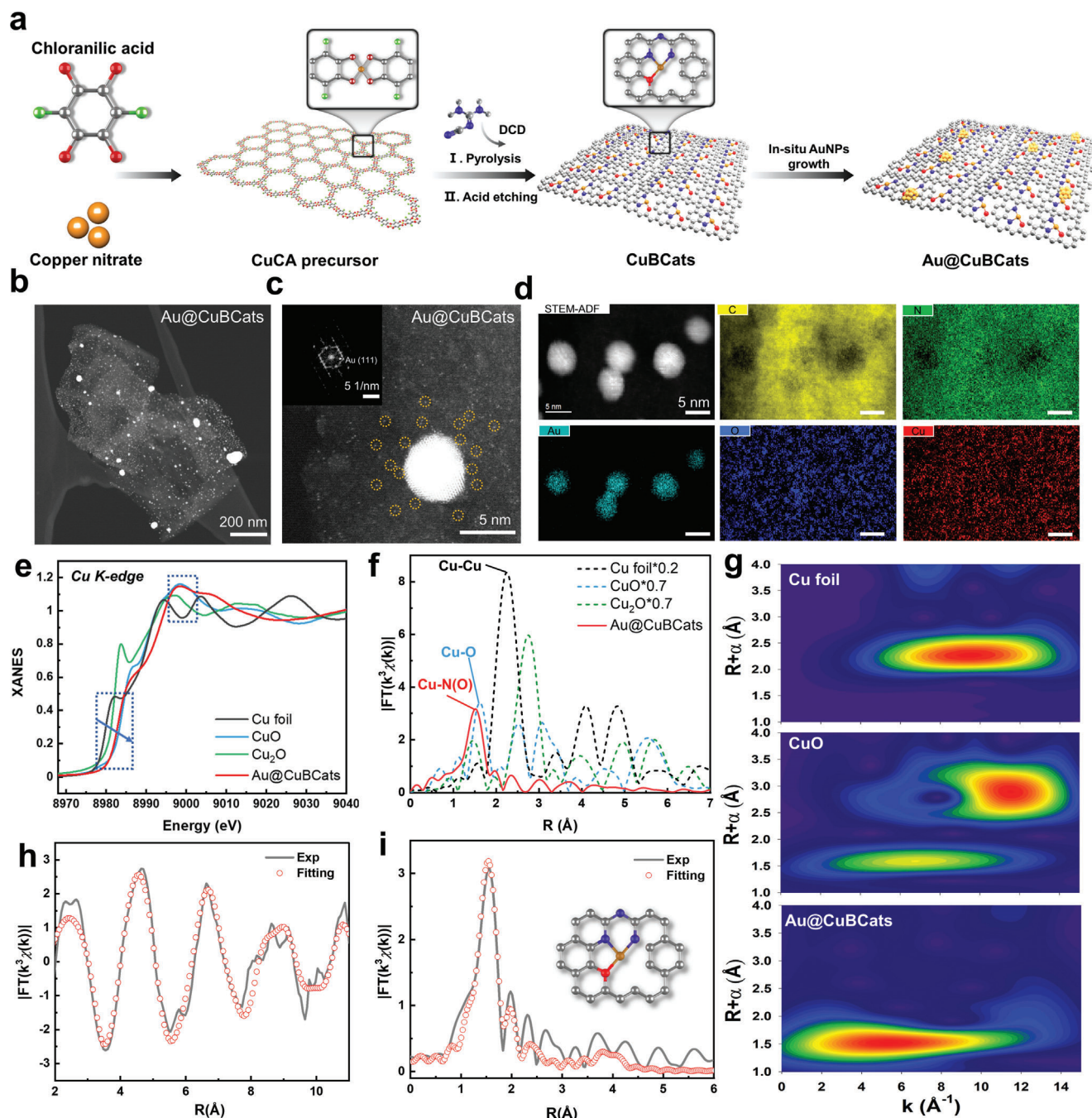
Figure 1. Synthesis and structural characterizations of Au@CuBCats. a) Schematic illustration of the synthesis of Au@CuBCats. b,c) STEM images of Au@CuBCats, on which the copper single-atoms are highlighted by yellow circles. Insert: Fast Fourier transform (FFT) pattern of gold nanoparticle. d) EDS mapping of Au@CuBCats. e,f) XANES and EXAFS spectra at Cu K-edge of Au@CuBCats. g) Wavelet transform of Cu foil, CuO, and Au@CuBCats. h,i) EXAFS fitting result of Au@CuBCats at k and R space, respectively.

of the Cu single atoms in Au@CuBCats, we measured X-ray absorption energy near-edge structure (XANES) of Cu foil, Cu_2O, CuO, and Au@CuBCats (Figure 1e). The results confirmed that the XANES of Au@CuBCats were located between those of Cu_2O and CuO, suggesting the valency of copper single-atoms was between +1 and +2. Subsequently, the extended X-ray absorption fine structure (EXAFS) was investigated to analyze the coordina-

tion configurations of the Cu sites. As shown in Figure 1f, the first coordination shell is located at 1.5 Å, suggesting Cu–N or/and Cu–O coordination. Meanwhile, no obvious Cu–Cu scattering at 2.2 Å was noticed in Au@CuBCats. Moreover, wavelet transform based on the EXAFS results was conducted to distinguish the backscattering atoms (Figure 1g). We observed the maximum intensity of Cu foil and CuO at 9.7 and 11.5 Å^{-1}, respectively, which
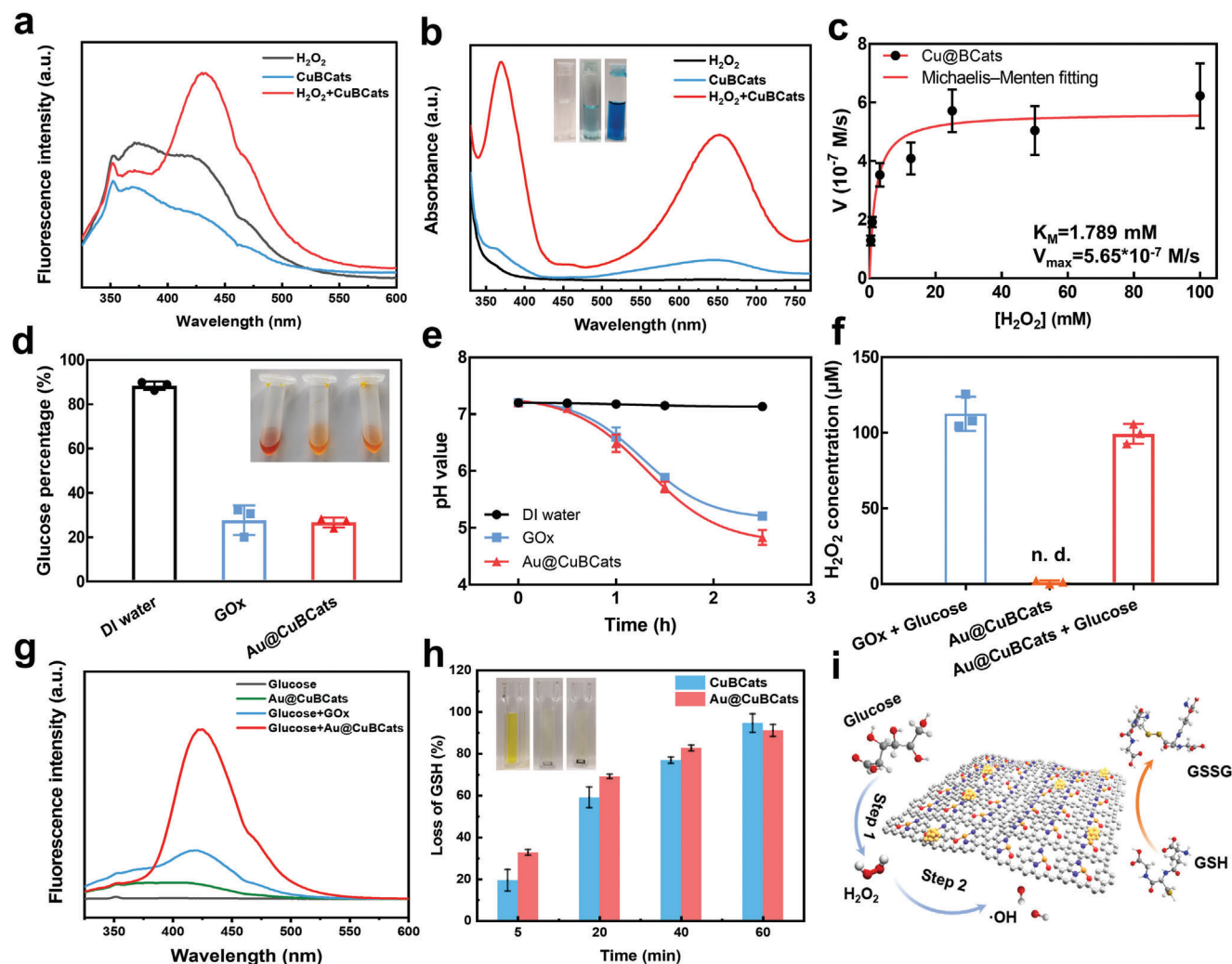
2301986 (3 of 11)

Figure 2. Catalytic performance of Au@CuBCats and CuBCats. a) Fluorescence spectroscopy in the presence of TA for measuring the OH generation property of CuBCats in the presence of H_2O_2, b) UV–Vis spectroscopy in the presence of TMB for characterizing peroxidase-like property, and c) Michaelis–Menten fitting curve of initial oxi-TMB generation velocities against H_2O_2 concentrations. d) Glucose percentage after 2 h incubation. e) The change of pH value with the increasing incubation time. f) H_2O_2 generation after 2 h incubation. n.d. represents non-detectable. g) OH generation property of Au@CuBCats in the presence of glucose. h) GSH consumption caused by Au@CuBCats and CuBCats. i) Schematic illustration of Au@CuBCats as a dual-enzyme-mimetic platform for initiating cascade catalysis and GSH depletion.

can be assigned to the Cu–Cu configuration. In comparison, the Au@CuBCats showed the maximum intensity at 5.2 Å^{-1}, which is assigned to Cu–N or/and Cu–O configuration. Although the copper was pre-anchored by oxygen in CuCA precursors, the coordinated O species also reacted with carbon and escaped under high temperatures.[25] Meanwhile, the N species generated from dicyandiamide would take over the vacancies during pyrolysis, thus assisting with anchoring the atomic Cu. Based on the synthesis procedures mentioned above, we speculate that both Cu–N and Cu–O exist in this structure. From the fitting result, we determined the coordination number (CN) of Cu–N(O) to be very close to three. Nevertheless, further unveiling the respective coordination number of N and O could be challenging due to the similar bond lengths of Cu–N and Cu–O. Therefore, in accordance with a previous study,[24] the back-scattering paths of N and O were simultaneously applied to obtain the best-fitting result; the fittings

with fixed CN of N and O were also compared (Table S2 and Table S3, Supporting Information). Upon fitting the EXAFS spectra to various structural models optimized with DFT, we confirmed that the best fit was obtained when the Cu center coordinated with one O atom and two N atoms (Figure 1 h,e). Therefore, the atomic Cu structure model of Au@CuBCats can be deduced; it is shown in the inset of Figure 1i.

Next, to study the OH generation property of bionanocatalysts, terephthalic acid (TA) was used as a probe since it can be oxidized by OH to generate the fluorescent compound TAOH, which can be easily detected by fluorescence spectroscopy under excitation at 315 nm. The significant TAOH signal at 430 nm confirms that CuBCats can catalyze H_2O_2 to generate abundant OH (**Figure 2**a). This OH generation can be attributed to the intrinsic POD-like activity of the atomic metal center.[26,27] Thus, a POD substrate, 3,3′,5,5′-tetramethylbenzidine (TMB) was used
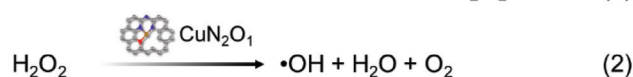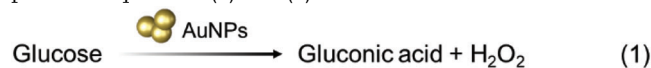
to study the POD-like property and steady-state catalytic kinetics. After 5 min of incubation, the TMB + H_2O_2 + CuBCats group became blue, with remarkable absorption peaks reflecting oxidized TMB at both 370 and 652 nm (Figure 2b). Then, we calculated the Michaelis–Menten constant (K_M) and the maximum initial velocity (V_{max}) to assess the catalytic efficacy of CuBCats (Figure 2c). The K_M value of the CuBCats was 1.789 mm for H_2O_2 substrate, indicating the higher affinity of CuBCats for H_2O_2 than that of HRP (3.70 mm for the H_2O_2 substrate).[28] Meanwhile, the V_{max} value of CuBCats showed around a 10-fold increase compared to HRP (V_{max} of HRP against H_2O_2 substrate is 8.71×10^{-8} m s^{-1}), suggesting the advanced POD-like performance of atomic copper sites.

After anchoring the AuNPs on CuBCats' surface, glucose was used to initiate the GOx-POD cascade catalytic process of Au@CuBCats. As shown in Figure 2d, a large amount of glucose consumption was noticed after a 2 h incubation with Au@CuBCats, almost equivalent to that of GOx, revealing the comparable glucose oxidative activity of Au@CuBCats (50 µg mL^{-1}) and GOx (2 U mL^{-1}). The downstream products-gluconic acid, H_2O_2, and OH were also examined by real-time pH meter, H_2O_2 assay kit, and TA measurement, respectively. We noticed a significant decrease in pH value over the incubation period (Figure 2e), revealing the generation of gluconic acid. Subsequently, we confirmed the generation of H_2O_2 in the Au@CuBCats + glucose group by H_2O_2 assay kit (Figure 2f). In agreement with TA measurements of CuBCats, we further demonstrated that Au@CuBCats can not only continuously catalyze the in situ-generated H_2O_2 to OH (Figure 2g), but also lead to the oxidation of TMB in the presence of glucose (Figure S7, Supporting Information). We did not notice a significant difference of DEM catalytic property of Au@CuBCats after exposing to air at room temperature over one month (Figure S8, Supporting Information). Moreover, glutathione (GSH), a common reducing agent in bacteria, was used as a model compound to test the intrinsic oxidative property of the catalysts. It was observed that the depletion rates of GSH were up to 94.66% and 91.11% at 60 min for CuBCats and Au@CuBCats, respectively, suggesting that these catalysts with single atomic copper sites have great power in weakening the bacterial antioxidant system and inducing oxidative stress. All of the above data confirm that the Au@CuBCats can catalyze the decomposition of glucose to OH via a dual-enzyme-mimetic cascade catalysis, and also further improve ROS treatment efficacy by depleting bacterial alternative oxidase (AOX).

The mechanism of how AuNPs catalyzes the oxidation of glucose to H_2O_2 has been studied both experimentally and theoretically.[21,29] For the further mechanistic understanding of the entire reaction, we performed DFT studies on the subsequent generation of OH from H_2O_2. Based on geometric fitting to our XAS data, we built a model of CuN_2O_1 embedded in graphene, as shown in Figure 1i. Upon characterizing the first-shell coordination geometry around Cu, we further considered that the N-containing precursor DCD exhibits the N–C–N–C–N connectivity (Figure S9, Supporting Information), prompting us to include an additional nitrogen dopant two atoms away from the coordination N. In fact, among the three possible arrangements of the CuN_2O_1 motifs, the motif shown is most stable only with the additional nitrogen dopant (Figure S10, Supporting Information). It is thus likely that this particular CuN_2O_1 arrangement, which fits best to the EXAFS data, is a result of bidentate coordination of DCD onto Cu during pyrolysis, while the remaining O originates from the initial coordination to CA. In addition to CuN_2O_1, other kinds of atomic copper sites were also calculated for comparison.

A proposed scheme of the reaction is shown in **Figure 3**a. The reaction starts from the adsorption of an H_2O_2 molecule. In the absence of solvent molecules, the geometry optimization of the H_2O_2-adsorbed led to the dissociation of H_2O_2 to form 2OH bound to CuN_2O_1. Although this already highlights the high catalytic activity of the Cu center, it cannot explain how OH radicals could be generated, since OH bound to Cu is unlikely to dissociate as radicals. Nevertheless, this contradiction is resolved by adding a single H_2O molecule to the calculations, upon which dissociation still occurs but the OH can be stabilized by H_2O in the *OH–H_2O–OH intermediate. With the assistance of H_2O, the OH is able to diffuse away from the reaction center instead of binding to Cu. For comparison of the dissociation kinetics, we further obtained the transition state for the dissociative step. In this mechanism, the OH that remains bound to the CuN_2O_1 site is unlikely to spontaneously desorb on its own as OH because of its strong binding (Figure S11, Supporting Information). Instead, the catalyst can be regenerated via protonation-reduction of *OH to form H_2O that finally desorbs. Since the evolution of O_2 was generated during the reaction (Figure S12, Supporting Information), we assumed the electrons originate from other H_2O_2 molecules and simulated the final reductive step at the standard reduction potential $U = E^0(O_2/H_2O_2) = 0.70$ V. Based on both experimental and theoretical results we mentioned above, the possible reaction mechanism of the cascading catalysis of was proposed as Equations (1) and (2):

$$\text{Glucose} \xrightarrow{\text{AuNPs}} \text{Gluconic acid} + H_2O_2 \quad (1)$$

$$H_2O_2 \xrightarrow{CuN_2O_1} \cdot OH + H_2O + O_2 \quad (2)$$

A combined free energy diagram, shown in Figure 3b, confirms that the reaction on the CuN_2O_1 site has a significantly lower energy barrier (0.44 eV) than that of CuN_4 (Figure 3b) and is thus more suitable for the H_2O_2 decomposition. In contrast, the dissociation of H_2O_2 on CuN_3 could be considered barrier-free, as the dissociation already occurs upon geometry optimization of the $H_2O_2(H_2O)$ intermediate. However, the instability of CuN_3 is reflected in the final reductive step, where the release of *OH would be inhibited. Therefore, in contrast to the other two motifs, CuN_2O_1 exhibits the ideal reactivity, one that is favorable for both the dissociation and desorption steps. Bader charge analysis showed the CuN_2O_1 center to be positively charged at +0.72 e, a value between those of CuN_4 (+1.11 e) and CuN_3 (+0.68 e). Generally, a more positively charged center implies a higher oxidation state of Cu and a lower tendency for releasing *OH,[22] consistent with the result for the OH-releasing step in the free energy diagram: the free energy for releasing *OH: $CuN_4 > CuN_2O_1 > CuN_3$. From the above results, we can conclude that the POD-like reaction pathway of atomic copper centers can be much improved by adjusting the copper coordination microenvironment.
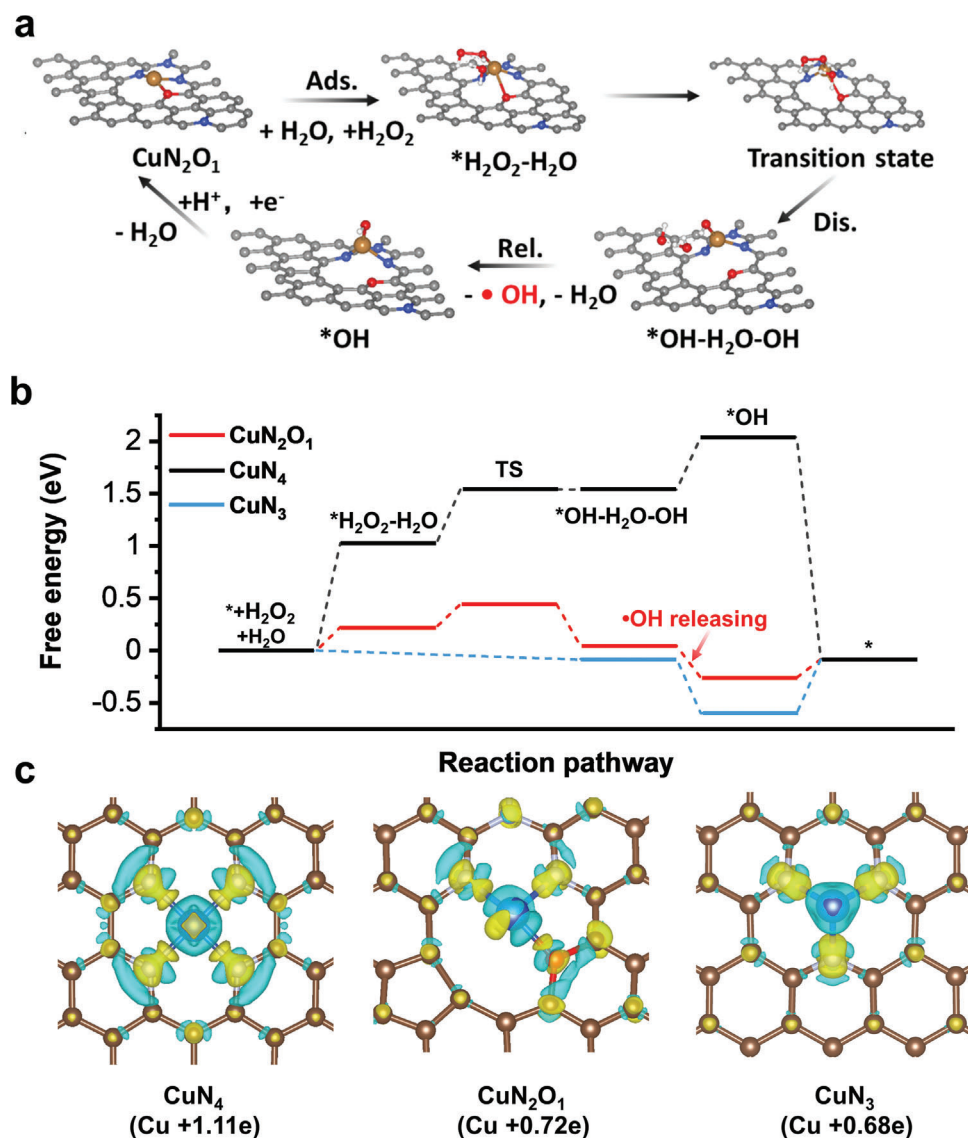
Figure 3. Mechanism of POD-like activity on CuN_2O_1 site. a) Scheme of the proposed reaction mechanism on CuN_2O_1 site. b) Free energy diagram for the reaction process on CuN_2O_1, CuN_4, and CuN_3 sites. c) Charge density difference plot and Bader charge of Cu in CuN_2O_1, CuN_4, and CuN_3 sites.

Encouraged by the above experimental and theoretical studies, we expect that the Au@CuBCats can serve as an ideal bactericidal agent in the presence of glucose via DEM cascade catalysis. To prove this concept, methicillin-resistant *Staphylococcus aureus* (*MRSA*, Gram-positive multidrug-resistant strain) and clinically isolated extended-spectrum *β*-lactamases producing *E. coli* (ESLP *E. coli*, a gram-negative MDR strain) were selected as presentative bacteria for the in vitro antibacterial study. As shown in **Figure** 4a, the bacterial colonies of both strains after treatment with Au@CuBCats were significantly smaller than those treated by PBS, glucose, glucose+GOx and glucose+CuBCats. Importantly, we noticed a significant difference (P < 0.0001) between glucose+GOx and glucose+Au@CuBCats groups (Figure 4c), attributable to the OH, generated by the cascade catalysis, further improving bactericidal performance.

Furthermore, we used SEM and confocal laser scanning microscope (CLSM) to investigate the antibacterial mechanism of Au@CuBCats from morphology and intracellular ROS level aspects, respectively. From SEM images (Figure 4b), we observed that the *MRSA* and ESLP *E. coli* exposed to the PBS, glucose and glucose+CuBCats maintained their original plump structures with intact outer membranes. After being treated with glucose+GOx, we noticed some distorted bacterial structures owing to the oxidative damage from H_2O_2. By contrast, in the group treated with glucose+Au@CuBCats, most of the bacteria suffered significant morphological deformations like collapse, distortion and breakage (highlighted by red arrows), indicating the highest bactericidal efficacy. Apart from the planktonic bacterial model, we also tested the antibiofilm performance. As shown in Figure S13 (Supporting Information), significant

**ADVANCED
SCIENCE NEWS**

www.advancedsciencenews.com

**ADVANCED
FUNCTIONAL
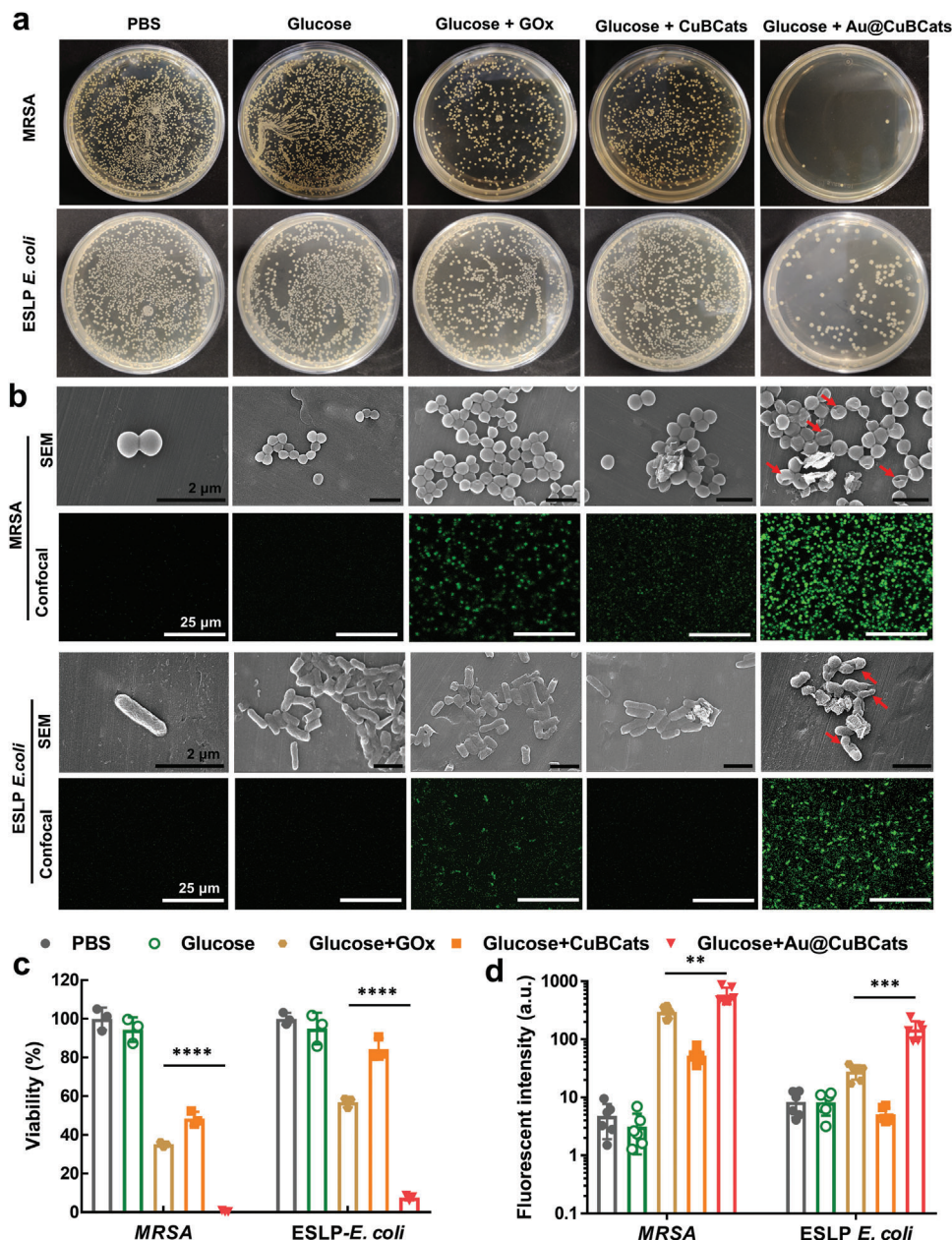MATERIALS**

www.afm-journal.de

Figure 4. In vitro bacterial killing profile of Au@CuBCats. a) Bacterial colonies after different treatments. b) SEM and CLSM images for bacterial cells after different treatments. Before confocal observation, the bacteria were dye-labelled by 2′,7′-dichlorodihydrofluorescein diacetate (DCF-DA) assay kit, which revealed the intracellular ROS level of bacteria. White scale bar: 25 µm. Black scale bar: 2 µm. c) Bacterial viability calculated from agar plates. The data are normalized to the PBS-treated group as 100% and presented as mean ± SD, n = 3. d) Semiquantitative statistics of intercellular ROS level of bacteria. The data are estimated from six fluorescent images by ImageJ. $^*p < 0.05$; $^{**}p < 0.01$; $^{***}p < 0.001$; $^{****}p < 0.0001$ by multiple t-tests for data in (c) and (d).

biofilm biomass reduction can be noticed for all Au@CuBCats treated groups. When the concentration was 800 µg mL^{-1}, Au@CuBCats were able to reduce 84.6% of biofilm, suggesting the robust antibiofilm effect. We then applied a fluorescent probe, namely DCF-DA, to further determine the intracellular ROS level of bacteria. Consistently, we found the highest intracellular ROS level for both strains in the glucose+Au@CuBCats treatment group (Figure 4b,d), suggesting that the highest oxidative stress was induced by OH. Interestingly, we also noticed that

the Au@CuBCats were able to effectively reduce the intracellular GSH level of MRSA (Figure S14, Supporting Information), leading to the oxidative stress.

Before conducting animal experiments, we first evaluated the biosafety of Au@CuBCats in both cellular and blood level. From CCK-8 results, we noticed the cell viability could fully recover to≈100% at day 3 after treatment by Au@CuBCats below 200 µg mL^{-1} (Figure S15, Supporting Information). Also, the Au@CuBCats exhibited no hemolytic effect even under high

concentration of 800 µg mL^{-1} (Figure S16, Supporting Information). Therefore, we are confident to further investigate the Au@CuBCats' ability for healing infected diabetic ulcers (**Figure 5**a). Wounds (6 mm in diameter) were inflicted on the ear of the diabetic rabbits and subsequently infected by *MRSA* to become ulcers. The formed diabetic ulcers were then randomly divided into four groups (n = 6 for each group) based on the following treatments: i) PBS; ii) CuBCats; iii) Vancomycin; iv) Au@CuBCats. To monitor the ulcer healing process, we photographed the ulcers every 4 days and the ulcer area was calculated from these images. As shown in Figure 5b and Figure S17 (Supporting Information), the vancomycin and Au@CuBCats groups recovered significantly faster and achieved 100% ulcer closure at day 11, when swollen ulcers were still observed in the PBS and CuBCats groups. Also, we found no viable *MRSA* colony for the vancomycin and Au@CuBCats groups (Figure 5c; Figure S18, Supporting Information). Consistent with these results, the bacterial number (BN) in the epidermis was calculated from the Giemsa staining (Figure 5d,e). Almost no bacterial cells were found in the epidermis for the vancomycin and Au@CuBCats groups, revealing that Au@CuBCats' bactericidal efficacy is as robust as that of vancomycin.

To further investigate the epidermis recovery and potential toxicity of Au@CuBCats at the tissue level after treatment, we collected the ulcer area and conducted systematic histological studies (Figure 5d,e). In order to determine inflammation levels in the ulcers after the different treatments, we applied hematoxylin and eosin (H&E) staining and immunofluorescence staining of proinflammatory cytokines including interleukin-1 beta (IL-1β) and tumor necrosis factor-alpha (TNF-α).[30] From H&E staining, we analyzed the inflammatory infiltration area (IIA) in ulcer tissues. Notably, the tissues of the Au@CuBCats and vancomycin groups exhibited well-ordered collagen structures and no apparent inflammation, properties similar to healthy tissues (Figure S19, Supporting Information). The absence of visible lesions demonstrates the good biosafety of Au@CuBCats treatment. By contrast, a great number of neutrophils and large IIA were observed for the tissues in the PBS and CuBCats groups, suggesting severe tissue inflammation originating from the surviving bacterial colonies. Compared to the PBS group, the vancomycin and Au@CuBCats groups showed very limited IL-1β expressions of 14.31% and 10.12%, respectively. In addition, significantly less TNF-α was found in the vancomycin (5.95%) and Au@CuBCats (6.59%) groups than in the PBS group. Besides, we did not find any lesion in major organs' H&E staining images (Figure S20, Supporting Information). These data confirmed the highly efficient therapeutic effect and good biosafety of the Au@CuBCats treatment.

The rebirth of collagen and vessels is an important indicator of tissue recovery.[31,32] Therefore, we used Masson's trichrome staining and cluster of differentiation 31 (CD31) immunofluorescence staining, respectively, to study the ulcer healing status via collagen deposition and neovascularization. The group treated with Au@CuBCats showed the highest collagen deposition area (CDA), suggesting the best collagen recovery. The CD31 expressions in the PBS and CuBCats groups were apparently limited as compared to the Au@CuBCats and vancomycin groups, with tissues still unrecovered from bacterial infection. Meanwhile, the Au@CuBCats and vancomycin groups had more than twice as many new vessels as the PBS group, confirming accelerated tissue healing. Taken together, these results demonstrate that Au@CuBCats can effectively cure bacterial diabetic ulcers in vivo and achieve accelerated regenerative ulcer healing. Also, as a ROS-based antibacterial therapy, the proposed Au@CuBCats have advantages like less possibility to arouse bacterial resistance, higher stability, and wider antibacterial spectrum as comparing to vancomycin. Therefore, we believe the Au@CuBCats show the potential as an antibiotic alternative for treating diabetic bacterial ulcers.

3. Conclusion

In conclusion, we synthesized a GOx-POD DEM bionanocatalyst Au@CuBCats. Via the DEM cascading catalysis by AuNPs and copper single atoms, the glucose can be catalyzed in situ to generate OH without extra energy input. Notably, the unique copper single atoms coordinated by one oxygen and two nitrogen atoms (CuN$_2$O$_1$) exhibit better POD catalytic performance than natural HRP. Further DFT calculations were performed to understand the catalytic mechanism and reveal the advantage of the CuN$_2$O$_1$ structure over other copper single-atom sites as both the dissociation of H$_2$O$_2$ and desorption of *OH are kinetically accessible. In vitro antibacterial results demonstrated that bionanocatalysts could induce significant bacterial reduction against the MDR bacterial strains *MRSA* and ESLP *E. coli*. In our in vivo study of bacterial diabetic ulcers in a rabbit ear model, the Au@CuBCats group exhibited rapid 100% recovery of the ulcer without any remaining inflammation lesion, suggesting the bionanocatalyst's outstanding therapeutic efficacy and biosafety. This work provides a proof of concept of a multi-enzyme mimetic bionanocatalyst serving as an MDR bacterial diabetic ulcer treatment. We also believe that this work will offer inspirations for designing the antibiotic-free bactericidal system and bionanocatalytic cascading medicines.

4. Experimental Section

Reagents: The chemical reagents including the cell culture materials were provided by commercial sources. All the reagents were of analytical grade and were used without further purification. ESLP *E. coli* was clinically isolated from patients in Charité and *MRSA* (ATCC 43 300) were purchased from American Type Culture Collection. Ultrapure water (18.2 MΩ; Millipore Co., USA) was applied in all experiments.

Instruments: STEM and EDX Mapping images were recorded by a JEOL JEM-ARM 200F scanning transmission electron microscope equipped with a cold field emission electron source, a DCOR probe corrector (CEOS GmbH), a 100 mm^2 JEOL Centurio EDX detector microscope. SEM images were obtained by using SU8030 scanning electron microscope (Hitachi). XAS spectra at the copper K-edge were collected at the BESSY synchrotron (Berlin, Germany) at beamlines KMC-3. The UV absorption spectra were recorded by M200 P Infinite PRO microplate reader (Tecan). The fluorescent spectra were measured by Fluorescence Spectrometer FP-6500 (Jasco). The fluorescence images were taken with Leica TCS SP8 CARS fluorescence confocal microscope.

Synthesis of CuBCats: Typically, 145 mg of copper nitrate hydrate and 1.044 g of chloranilic acid were separately dissolved in 50 mL methanol to get metal and ligand solution, respectively. Then, the metal solution was fast poured into the ligand solution under a high-speed magnetic stirring. The reaction was kept overnight. The products (CuCA precursors) were then washed with ethanol for three times by centrifugation and dried in an oven at 65 °C. Afterwards, the CuCA precursors were mixed with the
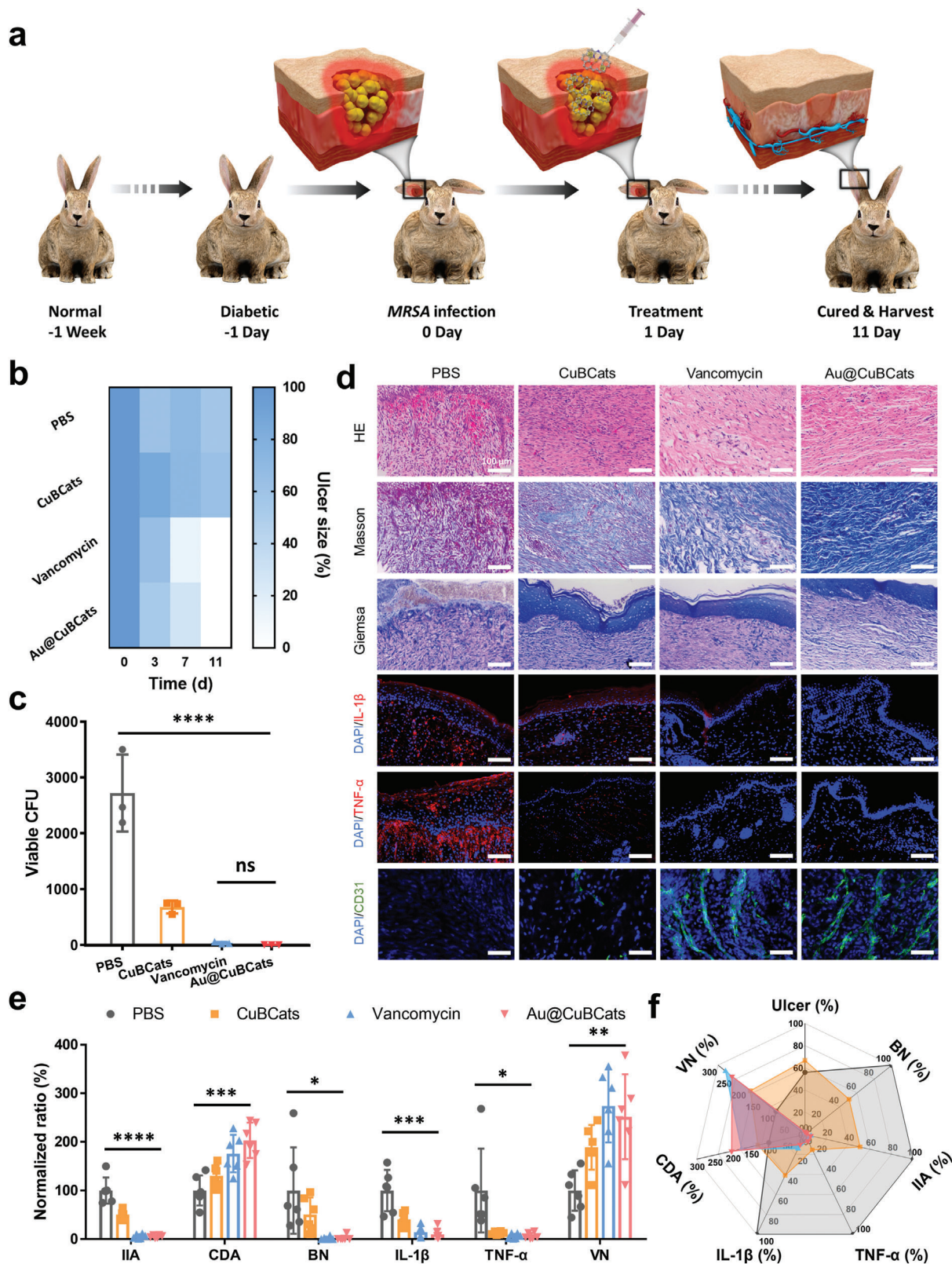
Figure 5. In vivo diabetic ulcer treatment with Au@CuBCats. a) Schematic illustration of the experimental flow. b) Ulcer size ratios with different treatments at days 0, 3, 7, and 11. c) Viable *MRSA* CFU on ulcer after 11 days of treatment. d) Immunohistochemical studies, and e) corresponding statistical analysis (normalized to PBS group) of diabetic ulcer collected from rabbit at day 11. Scale bar: 100 μm. f) Overall performance of PBS, CuBCats, vancomycin, and Au@CuBCats in the in vivo diabetic ulcer treatment. The data are estimated from six fluorescent images by ImageJ. $^{*}p < 0.05$; $^{**}p < 0.01$; $^{***}p < 0.001$; $^{****}p < 0.0001$ by multiple t test for data in (c) and (e), ns represents no significant difference.

**ADVANCED
SCIENCE NEWS**

www.advancedsciencenews.com

**ADVANCED
FUNCTIONAL
MATERIALS**

www.afm-journal.de

same mass amount of DCD in corundum boat and then subjected to a 900 °C-pyrolysis step for 3 h in a tube furnace, followed by an acid etching step using 1 M HCl under 90 °C overnight. Finally, the products were washed with water for three times by centrifugation and dried in an oven at 65 °C. We selected 900 °C as the carbonization temperature in order to local adjusting the copper single-atom structures. According to previous studies, when choosing 800 °C or a lower temperature for pyrolysis, metal-N_4 single-atom sites could be easily obtained. While a 900 °C carbonization temperature can facilitate the formation of unsaturated metallic single-atom sites, which possessed higher catalytic activities comparing to the symmetric metal-N_4 single-atom sites.[33–35]

Synthesis of Au@CuBCats: Typically, 1 mg of CuBCats were homogeneously dispersed in 1 mL of chloroauric acid ($HAuCl_4$) aqueous solution (2 mM) under the assistance of sonication. The oxygen-containing group within CuBCats could coordinate with Au ions via static interaction. Then, 62.5 μL of fresh prepared sodium borohydride aqueous solution (100 mM) was introduced to the above CuBCats-$HAuCl_4$ solution under vigorous magnetic stirring. The coordinated Au ions could then be in situ reduced on the CuBCats. After three times of water washing and drying, the final products, Au@CuBCats were obtained.

Computational Details: Spin-polarized DFT calculations were performed with the Vienna ab initio Simulation Package (VASP) in the framework of the projector-augmented wave (PAW) method with energy cutoff $E_{cut} = 600$ eV.[36,37] Geometry optimizations (including transition states) and frequency analyses were performed with the PBE functional, followed by single-point calculations with the PBE0 functional.[38] Grimme D3(BJ) dispersion correction with Becke-Johnson damping was applied to account for Van der Waals interactions.[39]

The RMM-DIIS algorithm was applied for electronic relaxation during geometry optimization while the conjugate gradient algorithm was applied, starting from the PBE wave function, for the single point calculation. The electronic convergence criterion was set to 10^{-5} eV. The Gaussian smearing approach with smearing width $\sigma = 0.05$ eV was applied. K-points were sampled using a $3 \times 3 \times 1$ Γ-centered mesh grid. Ionic relaxation steps were performed with the conjugate gradient algorithm with force convergence of 10^{-2} eV Å^{-1}. During geometry optimization, all atomic positions and the unit cell shape were optimized at constant unit cell volume (ISIF = 4). Transition states were obtained using the climbing image nudged elastic band (CI-NEB) method using nine images.[40]

Supporting Information

Supporting Information is available from the Wiley Online Library or from the author.

Conflict of Interest

The authors declare no conflict of interest.

Data Availability Statement

The data that support the findings of this study are available from the corresponding author upon reasonable request.

[1] Y. Zheng, S. H. Ley, F. B. Hu, *Nat Rev Endocrinol* **2018**, *14*, 88.
[2] P. Zimmet, K. G. Alberti, D. J. Magliano, P. H. Bennett, *Nat Rev Endocrinol* **2016**, *12*, 616.
[3] T. Wang, Y. Li, E. J. Cornel, C. Li, J. Du, *ACS Nano* **2021**, *15*, 9027.
[4] Y. Liang, M. Li, Y. Yang, L. Qiao, H. Xu, B. Guo, *ACS Nano* **2022**, *16*, 3194.
[5] C. M. Wong, K. H. Wong, X. D. Chen, *Appl. Microbiol. Biotechnol.* **2008**, *78*, 927.
[6] Y. Deng, X. Ouyang, J. Sun, X. Shi, Y. Li, Y. K. Chan, W. Yang, S. Peng, *Bioact Mater* **2022**, *25*, 748.
[7] T. Huang, B. Yuan, W. Jiang, Y. Ding, L. Jiang, H. Ren, J. Tang, *J. Mater. Chem. B* **2021**, *9*, 6190.
[8] Y. Zhu, J. Zhang, J. Song, J. Yang, Z. Du, W. Zhao, H. Guo, C. Wen, Q. Li, X. Sui, L. Zhang, *Adv. Funct. Mater.* **2020**, *30*, 1905493.
[9] C. Zhang, L. Zhang, W. Wu, F. Gao, R.-Q. Li, W. Song, Z.-N. Zhuang, C.-J. Liu, X.-Z. Zhang, *Adv. Mater.* **2019**, *31*, 1901179.
[10] C. Fang, Z. Deng, G. Cao, Q. Chu, Y. Wu, X. Li, X. Peng, G. Han, *Adv. Funct. Mater.* **2020**, *30*, 1910085.
[11] W. Xu, L. Jiao, Y. Wu, L. Hu, W. Gu, C. Zhu, *Adv. Mater.* **2021**, *33*, 2005172.
[12] G. Zhang, Y. Ji, X. Li, X. Wang, M. Song, H. Gou, S. Gao, X. Jia, *Adv Healthc Mater* **2020**, *9*, 2000221.
[13] X. Wan, H. Zhang, W. Pan, N. Li, B. Tang, *Chem. Commun.* **2021**, *57*, 5402.
[14] Y. Hu, S. Bai, X. Fan, F. Zhou, B. Chen, S. Tan, H. Xu, A. Pan, S. Liang, Y. He, *Biomater. Sci.* **2022**, *10*, 2358.
[15] C. Wu, K. Schwibbert, K. Achazi, P. Landsberger, A. Gorbushina, R. Haag, *Biomacromolecules* **2017**, *18*, 210.
[16] Y. Zhu, J. Zhang, J. Song, J. Yang, Z. Du, W. Zhao, H. Guo, C. Wen, Q. Li, X. Sui, *Adv. Funct. Mater.* **2020**, *30*, 1905493.
[17] C. J. Miller, Y. Chang, C. Wegeberg, C. J. McKenzie, T. D. Waite, *ACS Catal.* **2021**, *11*, 787.
[18] Q. Wang, J. Chen, H. Zhang, W. Wu, Z. Zhang, S. Dong, *Nanoscale* **2018**, *10*, 19140.
[19] J. Wang, R. Huang, W. Qi, R. Su, B. P. Binks, Z. He, *Appl. Catal., B* **2019**, *254*, 452.
[20] D. Bobo, K. J. Robinson, J. Islam, K. J. Thurecht, S. R. Corrie, *Pharm. Res.* **2016**, *33*, 2373.

[21] Y. Lin, Z. Li, Z. Chen, J. Ren, X. Qu, *Biomaterials* **2013**, *34*, 2600.

[22] X. Lu, S. Gao, H. Lin, L. Yu, Y. Han, P. Zhu, W. Bao, H. Yao, Y. Chen, J. Shi, *Adv. Mater.* **2020**, *32*, 2002246.

[23] Y. Sun, S. Mu, Z. Xing, J. Guo, Z. Wu, F. Yu, M. Bai, X. Han, C. Cheng, L. Ye, *Adv. Mater.* **2022**, *34*, 2206208.

[24] Y. Cai, J. Fu, Y. Zhou, Y.-C. Chang, Q. Min, J.-J. Zhu, Y. Lin, W. Zhu, *Nat. Commun.* **2021**, *12*, 586.

[25] H. Luo, L. Lari, H. Kim, S. Hérou, L. C. Tanase, V. K. Lazarov, M.-M. Titirici, *Nanoscale* **2022**, *14*, 910.

[26] B. Xu, H. Wang, W. Wang, L. Gao, S. Li, X. Pan, H. Wang, H. Yang, X. Meng, Q. Wu, L. Zheng, S. Chen, X. Shi, K. Fan, X. Yan, H. Liu, *Angew. Chem., Int. Ed.* **2019**, *58*, 4911.

[27] M. Huo, L. Wang, H. Zhang, L. Zhang, Y. Chen, J. Shi, *Small* **2019**, *15*, 1901834.

[28] L. Gao, J. Zhuang, L. Nie, J. Zhang, Y. Zhang, N. Gu, T. Wang, J. Feng, D. Yang, S. Perrett, X. Yan, *Nat. Nanotechnol.* **2007**, *2*, 577.

[29] P. Cheng, H. Wang, X. Shi, *Nanoscale* **2020**, *12*, 3050.

[30] C. Mao, W. Jin, Y. Xiang, Y. Zhu, J. Wu, X. Liu, S. Wu, Y. Zheng, K. M. C. Cheung, K. W. K. Yeung, *Adv. Funct. Mater.* **2022**, *32*, 2202887.

[31] X. Fan, X. Wu, F. Yang, L. Wang, K. Ludwig, L. Ma, A. Trampuz, C. Cheng, R. Haag, *Angew. Chem., Int. Ed.* **2022**, *61*, e202113833.

[32] L. Li, S. Cao, Z. Wu, R. Guo, L. Xie, L. Wang, Y. Tang, Q. Li, X. Luo, L. Ma, C. Cheng, L. Qiu, *Adv. Mater.* **2022**, *34*, 2108646.

[33] S. Ma, Z. Han, K. Leng, X. Liu, Y. Wang, Y. Qu, J. Bai, *Small* **2020**, *16*, 2001384.

[34] C. Yan, H. Li, Y. Ye, H. Wu, F. Cai, R. Si, J. Xiao, S. Miao, S. Xie, F. Yang, *Energy Environ. Sci.* **2018**, *11*, 1204.

[35] W. Zheng, J. Yang, H. Chen, Y. Hou, Q. Wang, M. Gu, F. He, Y. Xia, Z. Xia, Z. Li, *Adv. Funct. Mater.* **2020**, *30*, 1907658.

[36] G. Kresse, J. Hafner, *Phys. Rev. B* **1993**, *47*, 558.

[37] G. Kresse, J. Furthmüller, *Comput. Mater. Sci.* **1996**, *6*, 15.

[38] J. P. Perdew, K. Burke, M. Ernzerhof, *Phys. Rev. Lett.* **1996**, *77*, 3865.

[39] S. Grimme, S. Ehrlich, L. Goerigk, *J. Comput. Chem.* **2011**, *32*, 1456.

[40] G. Henkelman, B. P. Uberuaga, H. Jónsson, *Chem. Phys.* **2000**, *113*, 9901.

2301986 (11 of 11)